

Electrical control of the spatial uniformity of reactive species in plasmas

Mark A. Sobolewski^{a)} and Kristen L. Steffens

National Institute of Standards and Technology, Gaithersburg, Maryland 20899-8362

(Received 14 May 1999; accepted 2 July 1999)

We report a new method for controlling the spatial distribution of reactive chemical species in a parallel-plate plasma reactor, by means of a variable-impedance load placed between the unpowered electrode and ground. The technique was demonstrated in 89% CF₄/11% O₂ and 51% C₂F₆/49% O₂ chamber-cleaning plasmas at 13.3–133 Pa (0.1–1.0 Torr) in a Gaseous Electronics Conference Reference Cell. The rf current and voltage at both electrodes were measured, and plasma spatial characteristics were observed using two-dimensional (2D) planar laser-induced fluorescence of the CF₂ radical and 2D broadband optical emission measurements. By adjusting the load impedance to cancel the impedance of stray capacitances in parallel with the load, or the sheath capacitance in series with the load, the rf current at the load electrode could be made higher or lower than the current received when the electrode is grounded. When the rf current at the load electrode was minimized, regions of intense optical emission and high CF₂ density were shifted radially outward from the center of the reactor. When the rf current at the load electrode was maximized, regions of intense optical emission and high CF₂ density shifted radially inward, and the distribution of CF₂ across the electrode surfaces became more uniform. These results suggest that variable loads could be used to direct reactive species in chamber-cleaning plasmas to the surfaces most in need of cleaning, or to increase the radial uniformity of reactive species in etching plasmas.

[S0734-2101(99)00706-X]

I. INTRODUCTION

Fluorocarbon plasmas are widely used by the semiconductor industry to etch silicon oxide and nitride films, and to remove deposits of these materials from the walls of deposition chambers. In both etching and chamber cleaning, the spatial distribution of chemical species in the plasma is an important concern. In etching, the chemical and physical properties of the plasma should be as uniform as possible over the wafer area, to prevent overetching, underetching, or other damage. In chamber cleaning, however, uniformity is not necessarily the goal. Instead, the spatial characteristics of the plasma must be optimized to direct the active chemical species in the plasma to the chamber surfaces that are most in need of cleaning. Often, multiple cleaning steps are required to clean different surfaces: for example, a low pressure step to clean the outer regions of the reactor and one at somewhat higher pressure to clean regions closer to the center of the reactor.¹

In previous work^{2,3} the spatial characteristics of chamber-cleaning plasmas have been investigated in two capacitively coupled, parallel-plate reactors of identical design, known as the Gaseous Electronics Conference (GEC) Reference Cell,⁴ a standard platform designed to facilitate interlaboratory comparisons. In the first study² CF₄/O₂/Ar, C₂F₆/O₂/Ar, and NF₃/Ar plasmas were investigated. Although this study concentrated on power coupling, power absorption mechanisms, and other electrical issues, dramatic changes in the spatial uniformity of the plasmas, as a function of pressure, were observed and reported. In the second study³ the pressure dependence of the spatial characteristics of CF₄/O₂ and

C₂F₆/O₂ plasmas was investigated in detail, using planar laser-induced fluorescence (PLIF) of the CF₂ radical and broadband optical emission measurements. In both studies, changes in the spatial characteristics were correlated to changes in radio-frequency (rf) electrical measurements. In particular, plasmas with the greatest radial and axial uniformity were obtained at pressures which maximized the rf current at the upper, grounded electrode. In this article, we further investigate this correlation between electrical measurements and plasma spatial characteristics, using a variable-impedance load attached to the upper electrode of a GEC cell. By varying the load impedance, we are able to vary the current flow to the upper electrode—independent of pressure—and observe the resulting changes in plasma spatial characteristics.

Variable-impedance loads have been used previously^{5–7} to control ion bombardment energies in sputter-deposition tools. In those systems, rf current injected into the plasma at the rf-powered target electrode can flow to ground through several possible paths. It may flow to the substrate electrode or to the chamber walls or other reactor surfaces, depending on the impedance of each path. A variable load attached to the substrate electrode may be used to increase or decrease the rf current at that electrode. An increase in the rf current flowing to a surface from a plasma produces an increase in the voltage drop across the space-charge sheath region adjacent to the surface, which in turn provides greater acceleration to ions crossing the sheath. Increases in sheath current and sheath voltage should also produce increased heating of electrons near the sheath, according to models of electron heating processes.^{8–10} Because collisions with hot electrons contribute to the processes that create reactive species, one

^{a)}Electronic mail: mark.sobolewski@nist.gov

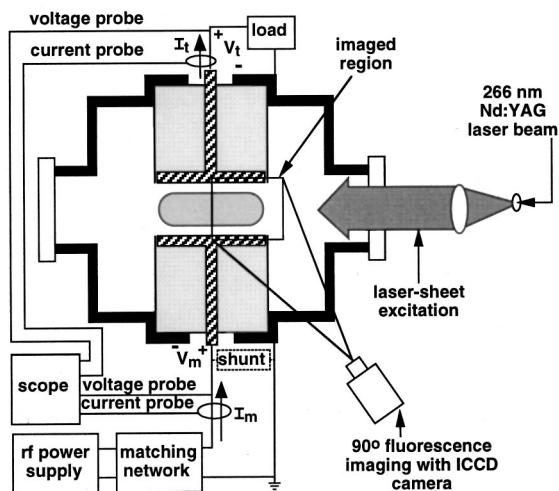


FIG. 1. Side view of the plasma reactor, showing the electrical probes and PLIF detection system.

might suspect that a variable load could also be used to control the density of reactive species near an electrode. Indeed, in this article we report observations in CF_4/O_2 and $\text{C}_2\text{F}_6/\text{O}_2$ plasmas that confirm this hypothesis. Two-dimensional (2D) images of the density of the CF_2 radical, obtained from PLIF, showed that the density and spatial distribution of the CF_2 radical can be controlled using a variable load. Similarly, 2D maps of broadband optical emission intensity showed that regions of excited species formation, which should correspond to regions of electron heating, can also be controlled. The effects we observe are rarely considered in the design, construction, or simulation of plasma reactors, and they have important implications. These implications, as well as possible applications, will be discussed.

II. EXPERIMENT

A. Plasma reactor

A diagram of the GEC cell in which the experiments were performed is shown in Fig. 1. It is a parallel plate, capacitively coupled reactor with 10.2 cm diameter, water-cooled, aluminum electrodes, separated by a gap of 2.25 cm. Each electrode is surrounded by an aluminum oxide insulator and a stainless steel ground shield. The lower electrode is powered by a 13.56 MHz power supply, coupled through a matching network equipped with an internal blocking capacitor. In previous studies performed in this reactor,^{3,11} the upper electrode was grounded to the outside of the vacuum chamber by a short piece of copper wire. Here, however, the copper wire was replaced by a variable-impedance load consisting of a coil in series with an air variable capacitor, mounted in an aluminum box.

Gases enter the cell through a showerhead arrangement of holes in the upper electrode. Gas flows were metered by calibrated mass flow controllers. Mixtures of 89% $\text{CF}_4/11\% \text{O}_2$ and 51% $\text{C}_2\text{F}_6/49\% \text{O}_2$ were used. (Percentages indicate mole percent.) The total flow rate was 7.1 $\mu\text{moles/s}$ (9.6 sccm) for CF_4/O_2 and 7.0 $\mu\text{moles/s}$ (9.4

sccm) for $\text{C}_2\text{F}_6/\text{O}_2$. A control valve on the exhaust line maintained the pressure in the cell at 13.3–133 Pa (100–1000 mTorr). The rf power at the powered electrode, excluding losses between the generator and the electrode, was about 30 W (see below) which corresponds to a power density of 0.37 W/cm^2 . This power density is comparable to industrial reactors operated at hundreds of watts, because of the larger size of industrial reactors and because external losses are usually not taken into account.

B. Optical measurements

Planar laser-induced fluorescence (PLIF) was performed to characterize the 2D relative spatial density of CF_2 in the plasma as a chemical marker of plasma uniformity. The PLIF technique has been discussed in detail previously.^{3,12} The 266 nm beam from an unseeded, quadrupled Nd:YAG laser was formed into a vertical sheet approximately 2.5 cm tall and 0.5 cm thick. The sheet was passed through the plasma, where it excited CF_2 radicals from the X (0,1,0) ground electronic state to the A (0,2,0) excited electronic state. Fluorescence between 300 and 400 nm, emitted by CF_2 as it dropped back down to the ground state, was collected normal to the laser sheet, using a gated, intensified charge-coupled device (ICCD) camera with a 105 mm, f/4.5 ultra-violet lens. Colored glass filters were used to reduce broadband plasma emission and to block the 266 nm scattered laser light. Averaging up to 4200 laser shots per image was necessary to obtain good signal to noise. Since PLIF detects only the CF_2 in the plane of the laser sheet, the spatial resolution was determined by the 5.0 mm laser sheet thickness and the $0.2 \text{ mm} \times 0.2 \text{ mm}$ imaged dimensions of the camera pixels. After each PLIF image, the laser was blocked, and an ICCD image of broadband, spontaneous plasma emission by multiple species between 300 and 400 nm was acquired over the same total time as the PLIF image and subtracted from the PLIF image. Emission, unlike PLIF, is a line-of-sight integrated measurement. Next, the PLIF images were normalized for spatial variations and drift in the laser intensity, and a uniform field correction¹³ was applied to the images to correct for any slight variations in collection efficiency across the ICCD.

We take the CF_2 PLIF intensity to be proportional to the electronic ground state density of CF_2 . We verified that collisional quenching does not affect the fluorescence yield,³ and low laser intensities ($\sim 0.4 \text{ mJ/cm}^2$) were used to keep the CF_2 PLIF signal in the linear regime. As discussed in detail in Ref. 3, temperature variations which could cause changes in PLIF intensity due to changes in ground state rotational and vibrational population distribution are believed to be small, especially under constant rf power conditions.

C. Electrical measurements

Electrical probes mounted on the reactor are shown in Fig. 1. The current and voltage on the lead that powers the lower electrode, $I_m(t)$ and $V_m(t)$, were measured by a Pear-

son 2877 current probe¹⁴ and a Phillips PM 8931 100:1 attenuating voltage probe.¹⁴ The current and voltage at a point between the upper electrode and the variable load, $I_t(t)$ and $V_t(t)$, were measured by another Pearson 2877 current probe¹⁴ and a Hewlett-Packard 10440A 100:1 voltage probe.¹⁴ Signals acquired by the probes were digitized by a Hewlett-Packard 54503A oscilloscope¹⁴ and transferred to a computer which extracted the magnitude and phase of Fourier components at the fundamental and harmonic frequencies. These magnitudes and phases are expressed as complex Fourier coefficients, denoted V_m , I_m , V_t , and I_t . Using procedures described previously¹⁵ phase errors caused by propagation delays in the lines connecting the probes to the oscilloscope were measured and accounted for.

To interpret the electrical data, one must first characterize the stray impedance of the reactor itself. A circuit model for the reactor is shown in Fig. 2. There, as in previous work,¹¹ the capacitances C_{pe} and C_m , inductance L_{pe} , and resistance R_{pe} are associated with the lower (powered) electrode assembly. The elements C_s , L_s , and R_s represent the tunable inductive shunt circuit^{4,15} which is adjusted to null the currents drawn by C_{pe} and C_m , so that the current drawn by the discharge itself can be measured more precisely. The variable-impedance load is represented by the elements C_v , L_v , and R_v , while C_{ue} , L_{ue} , R_{ue} , and C_t represent the upper electrode. The stray capacitance associated with the gap between the electrodes is C_g . The capacitance C_f is contributed by a thin insulating film on the surface of the upper electrode which has formed over the course of the cell's operation. No surface layer is present on the lower, powered electrode, because it is continually bombarded by highly energetic ions when the cell is operated. Finally, L_w is the self-inductance of the cavity which extends from the ground shields out to the wall of the vacuum chamber.

To obtain values for the circuit model, measurements were performed with no plasma ignited, with the cell powered by a variable-frequency rf power supply operated at 100 kHz–50 MHz. First, the lower electrode was powered by the variable-frequency supply and I_m and V_m were measured, with the lower electrode open-circuited and then short-circuited to its ground shield. Second, power was applied above the I_t and V_t probes (i.e., across the variable load) and I_t and V_t were measured, with the upper electrode open-circuited and then short-circuited to its ground shield. Third, to characterize the inductive load, I_t and V_t were measured with variable-frequency rf power applied just below the I_t and V_t probes. Values of the elements, except for C_g and L_w , were adjusted until an excellent fit to the measured parameters was obtained. The gap capacitance, C_g , was estimated using the equation $C_g = \epsilon_0 A/d$, where A is the electrode area and d is the electrode separation. For L_w , which is relatively unimportant in this study, and which depends solely on the chamber geometry, we used a value measured previously.¹¹ Values for the circuit elements are given in the caption to Fig. 2.

When the discharge is ignited, the measured signals, I_m , V_m , I_t , and V_t , include contributions from the reactor as

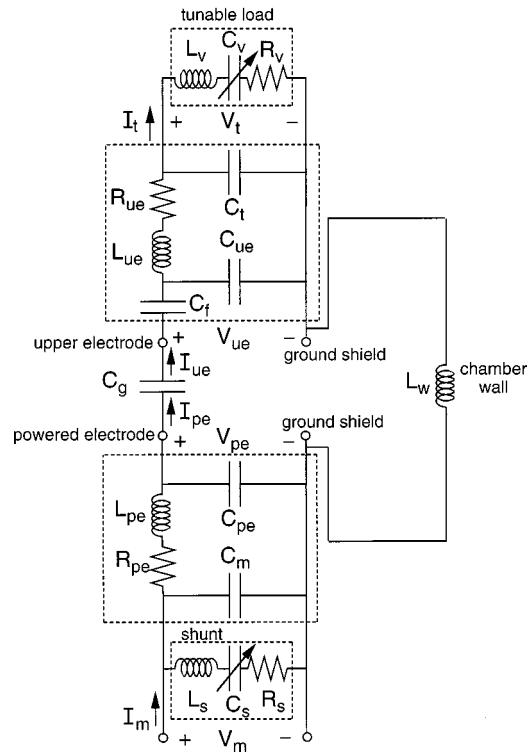


FIG. 2. Equivalent circuit model of the reactor. From measurements we obtain $C_{ue}=127$ pF, $L_{ue}=123$ nH, $R_{ue}=0.16$ Ω , $C_t=19$ pF, 21 pF $\leq C_v \leq 104$ pF, $L_v=2.45$ μ H, $R_v=0.5$ Ω , $C_f=3.2$ nF, $C_g=3.2$ pF, $C_{pe}=117$ pF, $L_{pe}=97$ nH, $R_{pe}=0.15$ Ω , $C_m=23$ pF, $C_s=99$ pF, $L_s=2.28$ μ H, $R_s=0.54$ Ω , and $L_w=36$ nH.

well as the discharge. It is therefore useful to transform the measured signals into signals that are more representative of the discharge itself. First, the current I_m and voltage V_m , measured on the power feed to the lower electrode, can be related to the current I_{pe} flowing into the plasma at the surface of the lower electrode and the voltage V_{pe} between the surface of the lower electrode and its ground shield, using the cascade matrix,¹⁵

$$\begin{bmatrix} V_{pe} \\ I_{pe} \end{bmatrix} = \begin{bmatrix} d & -b \\ -c & a \end{bmatrix} \begin{bmatrix} V_m \\ I_m \end{bmatrix}. \quad (1)$$

Here I_m , V_m , I_{pe} , and V_{pe} are the complex coefficients of Fourier components at a given angular frequency, ω , and a , b , c , and d are complex numbers called the cascade parameters.¹⁶ For the circuit model shown in Fig. 2, we obtain

$$a = 1 - \omega^2 L_{pe} C_{pe} + i\omega R_{pe} C_{pe}, \quad (2)$$

$$b = R_{pe} + i\omega L_{pe}, \quad (3)$$

$$c = i\omega C_{pe} + a(Y_s + i\omega C_m), \quad (4)$$

and

$$d = 1 + (R_{pe} + i\omega L_{pe})(Y_s + i\omega C_m), \quad (5)$$

where

$$1/Y_s = R_s + i\omega L_s + (i\omega C_s)^{-1}. \quad (6)$$

Similarly, I_t and V_t , the current and voltage measured on the lead that connects the upper electrode to the variable load, can be related to the current I_{ue} flowing from the plasma to the surface of the upper electrode and the voltage V_{ue} between the surface of the upper electrode and its ground shield, using

$$\begin{bmatrix} V_{ue} \\ I_{ue} \end{bmatrix} = \begin{bmatrix} h & f \\ g & e \end{bmatrix} \begin{bmatrix} V_t \\ I_t \end{bmatrix}, \quad (7)$$

where

$$e = 1 - \omega^2 L_{ue} C_{ue} + i\omega R_{ue} C_{ue}, \quad (8)$$

$$f = R_{ue} + i\omega L_{ue} + e/(i\omega C_f), \quad (9)$$

$$g = i\omega(C_{ue} + eC_t), \quad (10)$$

and

$$h = 1 - \omega^2 L_{ue} C_t + i\omega R_{ue} C_t + g/(i\omega C_f). \quad (11)$$

From the currents and voltages, one can define the impedances

$$Z_{pe} = V_{pe}/I_{pe}, \quad (12)$$

$$Z_{ue} = V_{ue}/I_{ue}, \quad (13)$$

and

$$Z_t = V_t/I_t, \quad (14)$$

where Z_{pe} is the combined impedance of everything downstream of the powered electrode, Z_t is the impedance of the variable load, and Z_{ue} is the impedance of the upper electrode including the variable load. If ϕ_{pe} is the phase of Z_{pe} (i.e., the phase of V_{pe} relative to I_{pe}) and ϕ_{ue} and ϕ_t are the phases of Z_{ue} and Z_t , then one can define the powers

$$P_{pe} = (1/2)|V_{pe}||I_{pe}|\cos\phi_{pe}, \quad (15)$$

$$P_{ue} = (1/2)|V_{ue}||I_{ue}|\cos\phi_{ue}, \quad (16)$$

and

$$P_t = (1/2)|V_t||I_t|\cos\phi_t. \quad (17)$$

Here, P_{pe} is the power flowing into the discharge from the lower electrode, P_t is power dissipated in the variable load, and P_{ue} is the power dissipated in the upper electrode and in the variable load. Although P_{pe} does not include power losses upstream of the powered electrode, it does include the power, P_{ue} , lost downstream. Thus, the power dissipated in the discharge itself is $P_{pe} - P_{ue}$.

We only report results at the fundamental frequency (13.56 MHz). Signals at harmonic frequencies were analyzed but they carried negligible power. Because the shunt circuit^{4,15} was tuned for 13.56 MHz, and because the circuit model parameters were chosen so that the model was forced to agree with measurements performed at 13.56 MHz, we were able to obtain the fundamental components of I_{pe} , V_{pe} , I_{ue} , and V_{ue} with essentially the same accuracy as I_m , V_m , I_t , and V_t . Random errors in the data are small because all parameters are obtained only after Fourier analyzing the waveforms, which suppresses noise. The total uncertainty is

dominated by systematic errors, which are contributed by the current probes (rated at $\pm 1\%$), the voltage probes (calibrated to $\pm 1\%$), the oscilloscope ($\pm 3\%$) and the phase calibration procedures ($\pm 1^\circ$). The total uncertainty is $\pm 4\%$ for all voltages and currents, $\pm 8\%$ for impedances, and $\pm 1^\circ$ for impedance phases. The total uncertainty of the power P_{pe} ranges from ± 2.5 W at $\phi_{pe} = 0^\circ$ to ± 4.0 W at $\phi_{pe} = 69^\circ$; the error in P_{ue} is at worst ± 0.4 W. Drift in the measurement system and reactor stray impedance was negligible, but during plasma operation small drifts in electrical parameters were observed. During the acquisition of the optical data, P_{pe} was stable within 0.4 W, I_{ue} and I_{pe} within 6 mA.

III. RESULTS

After installing the variable load and characterizing the reactor stray impedance, plasmas were ignited, and measurements were made at various settings of the variable load. For comparison, measurements were also performed with the load short circuited. This short-circuit condition is identical to the "grounded" condition in which the upper electrode was operated in previous studies, except for a small increase in L_{ue} due to modifications made to accommodate the load. Optical and electrical measurements obtained with the load short circuited were quite similar to previous results.³

In Sec. III A, we present a detailed description of plasma electrical parameters obtained by varying the tunable load over its entire range of operation, at a single pressure and gas mixture. An explanation of the principles of operation of the load, and how it affects the rf current flow through the plasma, is also provided. Then, in Sec. III B we present electrical and optical data for both CF_4/O_2 and C_2F_6/O_2 at varying pressures, demonstrating the ability of the load to control plasma spatial characteristics as well as the rf current.

A. Operation of the tunable load

When the tunable load is used, there is, in addition to pressure, power, and flow, another independent parameter. Strictly speaking, we vary C_v , the capacitance of the load, but a more convenient choice for the independent parameter is the total impedance of the load, Z_t , since it is obtained directly from the V_t and I_t measurements, using Eq. (14). From the circuit model shown in Fig. 2:

$$Z_t = R_v + i\omega L_v - i/(\omega C_v). \quad (18)$$

Another useful parameter is the load reactance, that is, the imaginary part of Z_t :

$$\text{Im}(Z_t) = |V_t||I_t|^{-1} \cos\phi_t = i\omega L_v - i/(\omega C_v), \quad (19)$$

which includes the inductive and capacitive terms in Z_t , but not the resistance. If $\text{Im}(Z_t) > 0$, the load has a net inductive impedance; if $\text{Im}(Z_t) < 0$, the load has a net capacitive impedance. Because its magnitude and sign are both meaningful, $\text{Im}(Z_t)$ is a more useful parameter than the magnitude, $|Z_t|$.

Figure 3 shows electrical data for a CF_4/O_2 discharge at 13.3 Pa (100 mTorr), obtained by varying the load over its entire range of operation. Plotted on the x axis is $\text{Im}(Z_t)$ from Eq. (19). By adjusting C_v , the variable capacitor in the load,

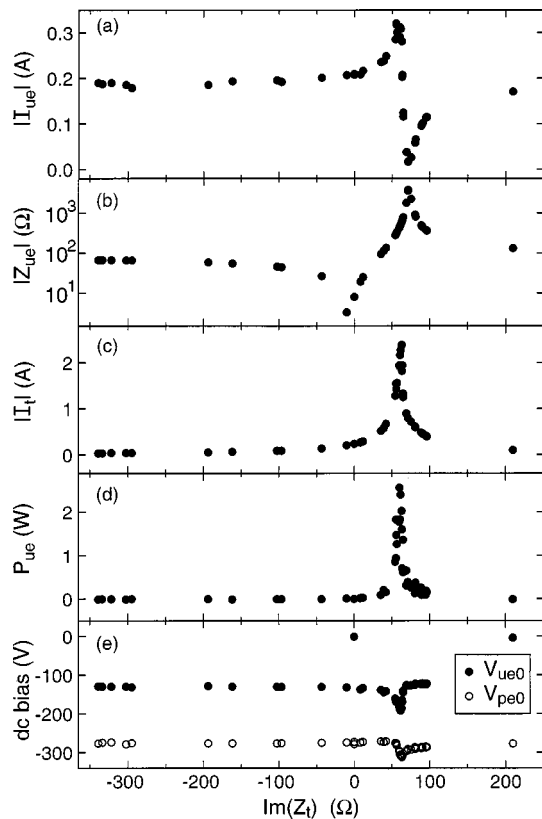


FIG. 3. Electrical parameters for a CF_4/O_2 discharge at 13.3 Pa (100 mTorr). As a function of $\text{Im}(Z_t)$, the imaginary part of the impedance of the tunable load, we plot (a) $|I_{ue}|$, the magnitude of the current at the upper electrode; (b) $|Z_{ue}|$, the magnitude of the impedance of the upper electrode combined with the tunable load; (c) $|I_t|$, the magnitude of the current flowing in the variable load; (d) P_{ue} , the power dissipated in the upper electrode and the tunable load; and (e) the dc self-bias voltage on the upper electrode, V_{ue0} , and on the lower electrode, V_{pe0} . During this experiment the power at the rf generator was held constant, P_{pe} varied from 28.4 to 33.7 W, and $|I_{pe}|$ varied from 418 to 490 mA.

$\text{Im}(Z_t)$ was varied from a negative (capacitive) impedance of -339Ω to a positive (inductive) impedance of $+96 \Omega$. By short-circuiting C_v , an additional point was obtained at 209Ω . Short circuiting the entire tunable load yields a data point at $\text{Im}(Z_t)=0 \Omega$. When the load is varied, the power at the lower electrode, P_{pe} , changes, unless the settings of the rf generator or the matching network are adjusted at each point. For simplicity, such adjustments were not made in Fig. 3; the settings of the rf generator and the matching network were held constant. For the data in Fig. 3, P_{pe} varied from 28.4 to 33.7 W, and $|I_{pe}|$ varied from 418 to 490 mA.

The current I_{pe} flowing from the powered electrode into the plasma may flow to the upper electrode, the upper ground shield, the lower ground shield, or the wall of the vacuum chamber. Figure 3(a) shows $|I_{ue}|$, the magnitude of the current that flows to the upper electrode. With the load short-circuited, $|I_{ue}|=209 \text{ mA}$. Using the tunable load, we were able to vary $|I_{ue}|$ far from this value, from a minimum of 17 mA to a maximum of 321 mA. The ratio $|I_{ue}|/|I_{pe}|$ could be varied from 4% to 69%, compared to 44% with the load short circuited.

Figure 3(b) shows $|Z_{ue}|$, the magnitude of the impedance of the upper electrode assembly including the tunable load, obtained from Eq. (13). Both a maximum and a minimum are observed. The maximum in $|Z_{ue}|$ coincides with the minimum in $|I_{ue}|$ observed in Fig. 3(a), because the high value of $|Z_{ue}|$ forces current to take other paths through the plasma. In contrast, the minimum in $|Z_{ue}|$ does not coincide with the maximum in $|I_{ue}|$, because $|I_{ue}|$ also depends on impedances within the discharge itself, in series with Z_{ue} . The maximum in $|I_{ue}|$ occurs at the minimum of the total impedance, not the minimum of $|Z_{ue}|$.

The sharp minima and maxima in Figs. 3(a) and 3(b) result from resonances, that is, the cancellation of inductive and capacitive impedances. There are two types of resonances, series and parallel. First consider a circuit consisting of an inductance L , a capacitance C , and a resistance R in series. The total impedance of the circuit is

$$Z = R + i\omega L - i/(\omega C). \quad (20)$$

Because the inductive and capacitive terms are of opposite sign, they may cancel, forcing $|Z|$, the magnitude of the impedance, to a minimum. At this “series resonance,” the current drawn by the circuit will be large, and the total voltage drop across the circuit will be small. In contrast, for three elements in parallel, the total impedance is

$$Z = [1/R - i/(\omega L) + i\omega C]^{-1}. \quad (21)$$

Now, if the inductive and capacitive terms cancel, $|Z|$ is maximized. At this “parallel resonance,” the circuit draws very little current.

The $|Z_{ue}|$ maximum and $|I_{ue}|$ minimum result from a parallel resonance of the net inductive impedance of the variable load with the parasitic capacitances C_{ue} and C_t (see Fig. 2). Although the circuit for the upper electrode is more complicated than that of Eq. (21), the situation is much the same. The current through the inductive load is equal and opposite to the sum of the currents through C_{ue} and C_t , so the total current, $|I_{ue}|$, is small and the combined impedance, $|Z_{ue}|$, is large.

The $|I_{ue}|$ maximum results from a series resonance between the net inductive impedance of the variable load (combined with the stray impedances) and the capacitive impedance of the sheath adjacent to the upper electrode. At resonance, the sheath capacitance and the inductive part of Z_{ue} cancel, so the total impedance from the powered electrode through the upper electrode to ground reaches a minimum value, limited only by the series resistances contributed by the discharge, the electrode, and the tunable load. Therefore, more current is drawn through the sheath to the upper electrode compared to other paths through the plasma, maximizing $|I_{ue}|$. At the maximum in $|I_{ue}|$, the magnitude of Z_{ue} is 309Ω , and its phase is $+83^\circ$, so it has a net inductive reactance, $\text{Im}(Z_{ue})=307 \Omega$. Therefore, we can infer that the sheath at the upper electrode has an equal and opposite capacitive reactance of -307Ω . In contrast, the minimum of $|Z_{ue}|$ is produced by another series resonance that only involves the inductances and capacitances in the upper electrode and the variable load. Although this resonance pro-

TABLE I. Electrical parameters for CF_4/O_2 discharges at three different pressures, p , with the tunable load adjusted to minimize or maximize $|I_{\text{ue}}|/|I_{\text{pe}}|$, (denoted “min” and “max”), and with the load short-circuited (“short”). $\text{Im}(Z_l)$ is the imaginary (i.e., inductive and capacitive) part of the load impedance; P_{pe} is the power flowing past the powered electrode into the discharge; P_{ue} is the power dissipated in the upper electrode and the tunable load; ϕ_{pe} is the phase of the impedance Z_{pe} , the combined impedance of everything downstream of the powered electrode; $|I_{\text{pe}}|$ is the magnitude of the current at the powered electrode; and $|I_{\text{ue}}|$ is the magnitude of the current at the upper electrode.

p (Pa)		$\text{Im}(Z_l)$ (Ω)	P_{pe} (W)	P_{ue} (W)	ϕ_{pe} (deg)	$ I_{\text{pe}} $ (mA)	$ I_{\text{ue}} $ (mA)	$ I_{\text{ue}} / I_{\text{pe}} $
13.3	min	71	32.2	0.3	-65	433	13	0.03
	short	0	31.3	0.0	-68	481	211	0.44
	max	59	31.5	1.8	-69	510	337	0.66
66.7	min	73	31.2	0.8	-32	383	3	0.07
	short	0	31.1	0.0	-47	559	408	0.73
	max	40	31.2	0.6	-38	576	469	0.82
133.3	min	74	30.8	1.5	-10	294	36	0.13
	short	0	30.8	0.0	-13	324	222	0.69
	max	29	31.2	0.1	-11	323	222	0.69

duces a small ($\sim 1 \Omega$) value for $|Z_{\text{ue}}|$, the magnitude of the sheath impedance is still large, 307 Ω or more. Thus, at the minimum of $|Z_{\text{ue}}|$, $|I_{\text{ue}}|$ is less than its maximum value.

The magnitude of the current flowing through the variable load, $|I_l|$, is plotted in Fig. 3(c). A maximum is observed in $|I_l|$ at a tuning position close to the maximum in $|I_{\text{ue}}|$. At the minimum in $|I_{\text{ue}}|$, $|I_l|$ is still rather large, but it is nearly exactly canceled by currents of opposite phase flowing through C_{ue} and C_l , making $|I_{\text{ue}}|$ small. When $|I_l|$ is large, the power dissipated in the tunable load and the upper electrode, P_{ue} , obtained from Eq. (16) and plotted in Fig. 3(d), is significant. Most of this power is dissipated in the tunable load itself, as can be shown by calculating the power P_l in Eq. (17). In contrast, at short circuit, i.e., at $\text{Im}(Z_l)=0$, $|I_l|$ and P_{ue} are much smaller. These results suggest that tunable loads should be designed to tolerate levels of current and power dissipation higher than the levels that are present when no tunable load is used. Also, it should be noted that any increase in the power P_{ue} means that there is less power available to be dissipated in the discharge. This loss can be compensated by increasing the power P_{pe} , to maintain $P_{\text{pe}} - P_{\text{ue}}$ constant, but, for the sake of simplicity, we did not do this in these experiments.

Finally, the dc bias on the upper electrode, V_{ue0} , is shown in Fig. 3(e), for comparison with the results of Logan⁵ and Lousa and Gimeno.⁷ The behavior of V_{ue0} is similar in some respects to Refs. 5 and 7. In particular, a minimum in V_{ue0} is observed which, as Logan and Lousa and Gimeno suspected, coincides with the maximum in $|I_{\text{ue}}|$. Like Logan, we are able to measure V_{ue0} despite having an insulating film on the electrode, perhaps because of defects in the film. Zero dc bias is measured at two points in Fig. 3(e). At these points, obtained by short circuiting the load capacitor or the entire load, there is a dc connection between the upper electrode and ground which forces V_{ue0} to zero. Aside from these two points, V_{ue0} in Fig. 3(e) is always strongly negative, unlike Refs. 5 and 7, where weakly negative and positive dc biases were obtained. This difference can be explained by the

CF_4/O_2 discharge being much more electronegative than the Ar or Ar/ N_2 discharges studied previously. In the electronegative gases the discharge is confined to the center of the reactor, producing a more symmetric sharing of the dc bias between both electrodes. The dc bias on the powered electrode, V_{pe0} , is also seen in Fig. 3(e) to vary with tuning position, presumably because of changes in the plasma potential which occur as the tunable load is adjusted.

B. Electrical control of plasma uniformity

Electrical parameters measured as a function of pressure are shown in Table I for CF_4/O_2 and Table II for $\text{C}_2\text{F}_6/\text{O}_2$. For each pressure, measurements were performed with the variable load adjusted to maximize $|I_{\text{ue}}|/|I_{\text{pe}}|$, with the load adjusted to minimize $|I_{\text{ue}}|/|I_{\text{pe}}|$, and with the load short circuited. At each data point, the power at the rf generator was adjusted to maintain P_{pe} as nearly constant as possible. At short circuit, as in previous studies,^{2,3} $|I_{\text{ue}}|/|I_{\text{pe}}|$ rises when the pressure is increased from 13.3 to 66.7 Pa (100–500 mTorr) and then falls when the pressure is further increased to 133 Pa (1000 mTorr). At 13.3–66.7 Pa (100–500 mTorr) $|I_{\text{ue}}|$ and $|I_{\text{ue}}|/|I_{\text{pe}}|$ may be increased or decreased by appropriately tuning the variable load. At 133 Pa (1000 mTorr), however, no increase in $|I_{\text{ue}}|/|I_{\text{pe}}|$ could be obtained: tuning the load for maximum $|I_{\text{ue}}|/|I_{\text{pe}}|$ gave the same value of $|I_{\text{ue}}|/|I_{\text{pe}}|$ obtained at short circuit. This suggests that the sheath at the upper electrode becomes resistive rather than capacitive at high pressures. As discussed above, the increase in $|I_{\text{ue}}|$ depends on the inductance of the variable load (combined with the upper electrode assembly) canceling the capacitance of the sheath. The resistance of the sheath, however, cannot be canceled. It is also possible that the sheath capacitance is dominated by a much larger series resistance contributed by the plasma. This explanation is supported by the observation, seen in Tables I and II and in previous studies,^{2,3} that the phase of the plasma impedance, ϕ_{pe} ,

TABLE II. Electrical parameters for C_2F_6/O_2 discharges, as defined in Table I.

p (Pa)		$\text{Im}(Z_p)$ (Ω)	P_{pe} (W)	P_{ue} (W)	ϕ_{pe} (deg)	$ I_{pe} $ (mA)	$ I_{ue} $ (mA)	$ I_{ue} / I_{pe} $
13.3	min	72	30.8	0.6	-58	452	18	0.04
	short	0	30.8	0.0	-63	500	233	0.47
	max	57	31.2	1.6	-64	571	360	0.63
53.3	min	72	31.1	1.8	-22	356	31	0.09
	short	0	31.2	0.0	-34	486	373	0.77
	max	34	30.8	0.5	-28	496	400	0.81
133.3	min	75	31.3	1.2	-4	262	53	0.20
	short	0	31.1	0.0	-1	264	112	0.42
	max	17	31.2	0.0	0	264	115	0.44

shifts from capacitive phases (near -90°) at low pressures towards more resistive phases (near 0°) at high pressures. The minimum in $|I_{ue}|/|I_{pe}|$ can still be obtained at high pressures, since it does not depend on any property of the sheath. It only requires that impedances external to the plasma be tuned to produce a high-impedance, parallel-resonant state.

At each set of conditions given in Tables I and II, PLIF and optical emission measurements were performed. For

CF_4/O_2 at 66.6 Pa (500 mTorr), two-dimensional contour maps of CF_2 density obtained by PLIF are shown in Fig. 4. When the tunable load is short circuited, in Fig. 4(b), the CF_2 density peaks at an axial position midway between the electrodes, and at a radial position roughly two thirds of the way out to the electrode edge. When $|I_{ue}|/|I_{pe}|$ is minimized, in Fig. 4(a), the maximum in CF_2 density is shifted vertically

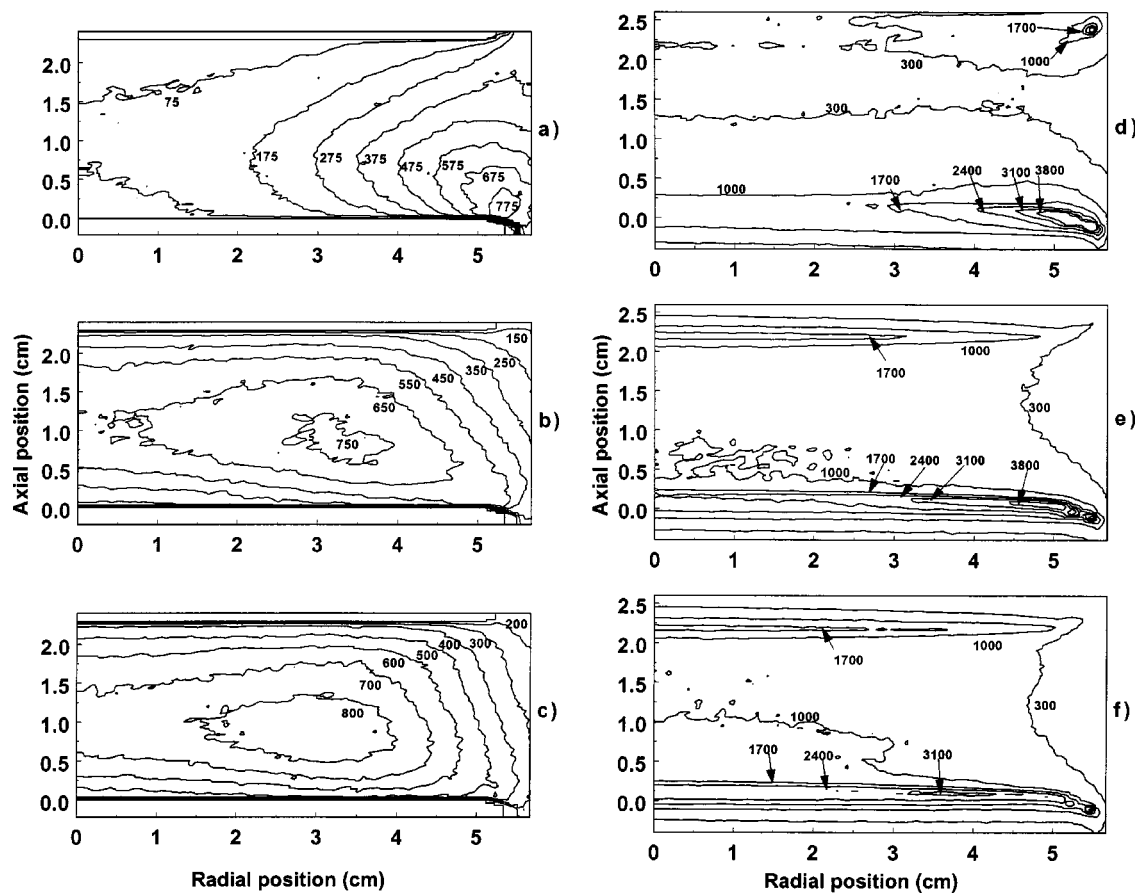


FIG. 4. Contour maps for (a)–(c) PLIF measurement of CF_2 density and (d)–(f) broadband optical emission intensity for a CF_4/O_2 discharge at 66.7 Pa (500 mTorr), obtained with (a),(d) the tunable load adjusted to minimize $|I_{ue}|/|I_{pe}|$; (b),(e) the tunable load short circuited; and (c),(f) the tunable load adjusted to maximize $|I_{ue}|/|I_{pe}|$. Outlines of the upper and lower electrodes are shown in (a)–(c). Load settings, currents, and powers are given in Table I. All PLIF contour values in (a)–(c), Figs. 5–7, and Figs. 8(a)–8(c) use the same intensity scale, in arbitrary units. Emission intensity contour values in (d)–(f) and Figs. 8(d)–8(f) use a common intensity scale, in arbitrary units, different from the PLIF scale.

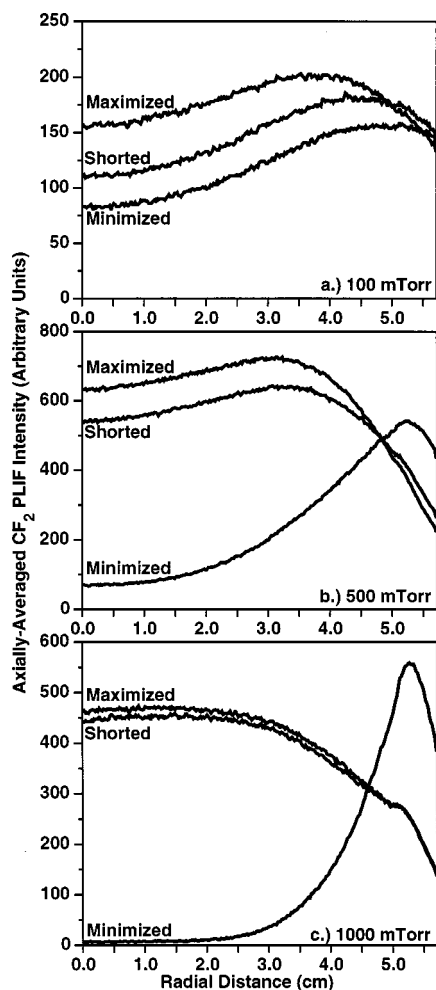


FIG. 5. Plots of PLIF measurement of CF_2 density averaged in the axial (i.e., vertical) direction, as a function of radial position, in CF_4/O_2 discharges at (a) 13.3 Pa (100 mTorr); (b) 66.7 Pa (500 mTorr); and (c) 133 Pa (1000 mTorr), for three different settings of the variable load. Load settings, currents, and powers are given in Table I.

and radially to a position close to the edge of the powered electrode. In contrast, when $|I_{\text{ue}}|/|I_{\text{pe}}|$ is maximized, in Fig. 4(c), the peak in CF_2 density shifts slightly inward. At radial positions close to the center, the CF_2 density decreases when $|I_{\text{ue}}|/|I_{\text{pe}}|$ is minimized, and increases when $|I_{\text{ue}}|/|I_{\text{pe}}|$ is maximized. At positions far from the center, the trends are reversed. To accentuate the radial changes, the CF_2 densities in Figs. 4(a)–4(c) were averaged in the vertical direction and are plotted versus radial position in Fig. 5(b). The shifts in the peak of the CF_2 distribution and the changes at each radial position are clearly observed.

Additional information can be obtained from the contour maps of broadband optical emission, shown in Figs. 4(d)–4(f). Electron impact dissociation and electronic excitation of molecules in the plasma results in electronically excited molecular fragments and atoms which subsequently emit. Because the lifetimes of the excited state fragments are short (e.g., 61 ± 3 ns for CF_2),¹⁷ they emit before they can travel far from the region in which they were created. Thus, the spatial distribution of optical emission intensity indicates

where reactive species, including CF_2 , are created. Also, because energetic electrons are necessary to create the fragments, regions of higher optical emission intensity indicate regions where higher densities of hot electrons are present.

In Figs. 4(d)–4(f), high optical emission intensities are observed primarily near the electrode and ground shield surfaces. Presumably, hot electrons are produced near these surfaces either by ohmic heating in the presheath region, stochastic heating at the boundary between the presheath and the sheath, or heating of secondary electrons within the sheath and presheath. In any of these heating mechanisms,⁸ an increase in rf current density produces an increase in electron heating. Thus, the changes in emission intensity seen in Figs. 4(d)–4(f) can be explained by changes in the path taken by the rf current. When the tunable load is short circuited, in Fig. 4(e), local maxima in the optical emission intensity are observed near the edge of the lower electrode and close to the center of the upper electrode. When $|I_{\text{ue}}|/|I_{\text{pe}}|$ is minimized, in Fig. 4(d), the feature near the upper electrode disappears, and instead a local maximum appears near the ground shield of the upper electrode, at $r = 5.5$ cm. Going from Figs. 4(e) to 4(d), $|I_{\text{ue}}|$ falls from 408 to 3 mA, which minimizes or even eliminates heating of electrons near the upper electrode. Presumably, some of the current rejected from the upper electrode flows to its ground shield, resulting in increased heating of electrons and optical emission near the shield. Some of the current rejected from the upper electrode probably flows to the lower electrode ground shield, as well. Emission intensity near the center of the powered electrode is lower in Fig. 4(d), when $|I_{\text{ue}}|/|I_{\text{pe}}|$ is minimized, than in Fig. 4(e), where the load is short circuited. This may indicate a redistribution of the current density along the powered electrode. In Fig. 4(d), where the current flows predominantly to the ground shields, the current density at the lower electrode may be peaked at a larger radius than in Fig. 4(e), where most of it flows straight across the gap to the upper electrode. When $|I_{\text{ue}}|/|I_{\text{pe}}|$ is maximized, in Fig. 4(f), the optical emission intensity near the lower electrode becomes more radially uniform, and its maximum shifts radially inward to $r = 3.7$ cm. These changes suggest that the current density at the lower electrode becomes more radially uniform when $|I_{\text{ue}}|/|I_{\text{pe}}|$ is maximized. Changes at the upper electrode are much less noticeable in Figs. 4(e) and 4(f). Going from Fig. 4(e) to 4(f), $|I_{\text{ue}}|$ only changes from 408 to 469 mA and $|I_{\text{ue}}|/|I_{\text{pe}}|$ only changes from 73% to 82%.

PLIF data obtained in CF_4/O_2 plasmas at 133 Pa (1000 mTorr) are shown in Fig. 6. When the tunable load is shorted, in Fig. 6(b), two local maxima in CF_2 density are observed: one near the center of the electrodes and another near the edge of the powered electrode. The latter illustrates the tendency of discharges in CF_4/O_2 and other electronegative gases to “collapse” as the pressure increases. At sufficiently high pressures, in CF_4/O_2 , $\text{C}_2\text{F}_6/\text{O}_2$, or NF_3/Ar discharges, the plasma glow contracts to a small, ring-like region between the powered electrode and its ground shield.^{2,3} This collapse is accompanied by a decrease in $|I_{\text{ue}}|/|I_{\text{pe}}|$, as more of the current at the powered electrode

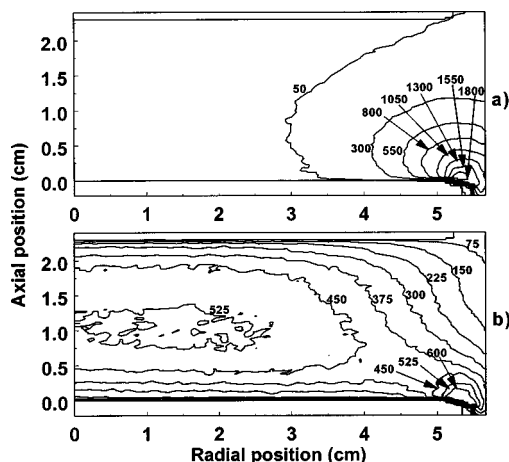


FIG. 6. Contour maps for PLIF measurement of CF_2 density for a CF_4/O_2 discharge at 133 Pa (1000 mTorr), obtained with (a) the tunable load adjusted to minimize $|I_{ue}|/|I_{pe}|$; and (b) the tunable load short circuited. Load settings, currents, and powers are given in Table I.

flows to its ground shield, and less flows to the upper electrode.^{2,3} The collapse can be accelerated by tuning the load to minimize the current at the upper electrode, as shown in Fig. 6(a). We were not able to forestall the collapse of the discharge by adjusting the load to maximize $|I_{ue}|/|I_{pe}|$, however. At 133 Pa (1000 mTorr) PLIF images obtained with $|I_{ue}|/|I_{pe}|$ maximized were very similar to what was obtained with the electrode shorted [Fig. 6(b)], as were the $|I_{ue}|$ and $|I_{ue}|/|I_{pe}|$ values themselves (see Table I). Presumably, this is because the sheath at the upper electrode is resistive rather than capacitive at 133 Pa (1000 mTorr), as discussed above. When the data from Fig. 6 are averaged in the vertical direction and plotted versus radial position, in Fig. 5(c), the changes in the radial uniformity are also clearly observed. Optical emission images at 133 Pa CF_4/O_2 appeared similar to data at 66.7 Pa (500 mTorr), in Figs. 4(d)–4(f).

In contrast, at lower pressures, CF_4/O_2 discharges tend to expand into regions beyond the edge of the electrodes, outside the field of view of the ICCD camera. This expansion is accompanied by a decrease in $|I_{ue}|/|I_{pe}|$.^{2,3} Presumably, the expansion coincides with the opening of additional current paths to more remote portions of the ground shields (and perhaps also to the wall of the vacuum chamber) so that a smaller fraction of $|I_{pe}|$ is drawn by the upper electrode. The expansion can be counteracted by adjusting the tunable load to maximize $|I_{ue}|/|I_{pe}|$, as can be seen in Fig. 7, where PLIF data from 13.3 Pa (100 mTorr) CF_4/O_2 are shown. When the upper electrode is short circuited, in Fig. 7(b), the peak in CF_2 density occurs at $r=4.5$ cm. When $|I_{ue}|/|I_{pe}|$ is maximized, in Fig. 7(c), the peak in CF_2 density moves radially inward, to 3.5 cm, and the CF_2 density increases throughout nearly the entire field of view. This increase occurs despite an increase in P_{ue} , the power lost in the upper electrode, and a slight decrease in $P_{pe}-P_{ue}$, the total power delivered to the discharge, from 31.3 to 29.7 W (see Table I). In contrast, when $|I_{ue}|/|I_{pe}|$ is minimized, in Fig. 7(a), the CF_2 density decreases throughout nearly the entire field of view. The

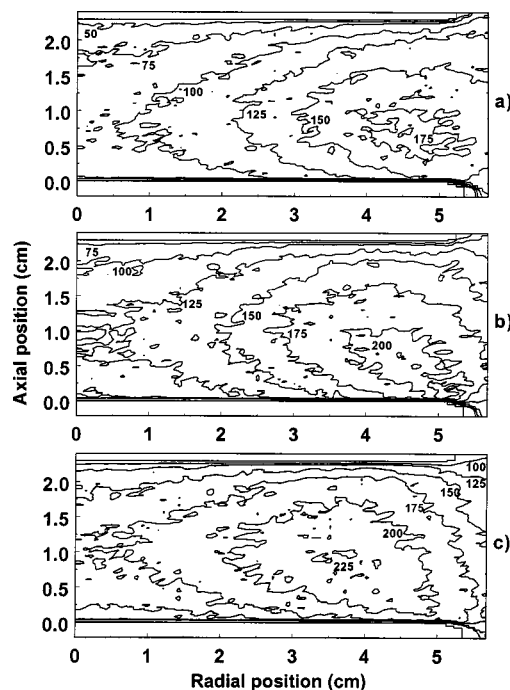


FIG. 7. Contour maps for PLIF measurement of CF_2 density for a CF_4/O_2 discharge at 13.3 Pa (100 mTorr), obtained with (a) the tunable load adjusted to minimize $|I_{ue}|/|I_{pe}|$; (b) the tunable load short circuited; and (c) the tunable load adjusted to maximize $|I_{ue}|/|I_{pe}|$. Load settings, currents, and powers are given in Table I.

shape of the CF_2 distribution in Fig. 7(a) is similar to Fig. 7(b). The radial shifts and overall changes in intensity seen in Fig. 7 are also visible in Fig. 5(a), where the data have been averaged in the axial direction.

For $\text{C}_2\text{F}_6/\text{O}_2$ discharges at the same pressure, 13.3 Pa (100 mTorr), similar behavior is observed. When $|I_{ue}|/|I_{pe}|$ is minimized, in Fig. 8(a), the CF_2 density decreases from the levels observed when the upper electrode is shorted, in Fig. 8(b), and the peak in CF_2 density shifts out to a larger radius. When $|I_{ue}|/|I_{pe}|$ is maximized, in Fig. 8(c), the CF_2 density increases and the peak in CF_2 density shifts inward, closer to the radial center.

Figure 8 also shows corresponding optical emission images. As in Fig. 4, strong changes are observed near the upper electrode. When the upper electrode is shorted, in Fig. 8(e), a weak maximum in emission is observed near the upper electrode. When $|I_{ue}|/|I_{pe}|$ is minimized, in Fig. 8(d), this feature is eliminated. When $|I_{ue}|/|I_{pe}|$ is maximized, in Fig. 8(f), the feature becomes much stronger. The emission maximum near the lower electrode shifts radially outward when $|I_{ue}|/|I_{pe}|$ is minimized, and inward when $|I_{ue}|/|I_{pe}|$ is maximized. These radial shifts, like the shifts observed in Figs. 4(d)–4(f), suggest that changes are occurring in the way the rf current is distributed across the surface of the electrodes. Close examination shows that the peak near the upper electrode shifts down, away from the upper electrode, going from Fig. 8(e) to 8(f). When the current at the top electrode is maximized, in Fig. 8(f), the voltage across the sheath adjacent to the top electrode and the thickness of this sheath are

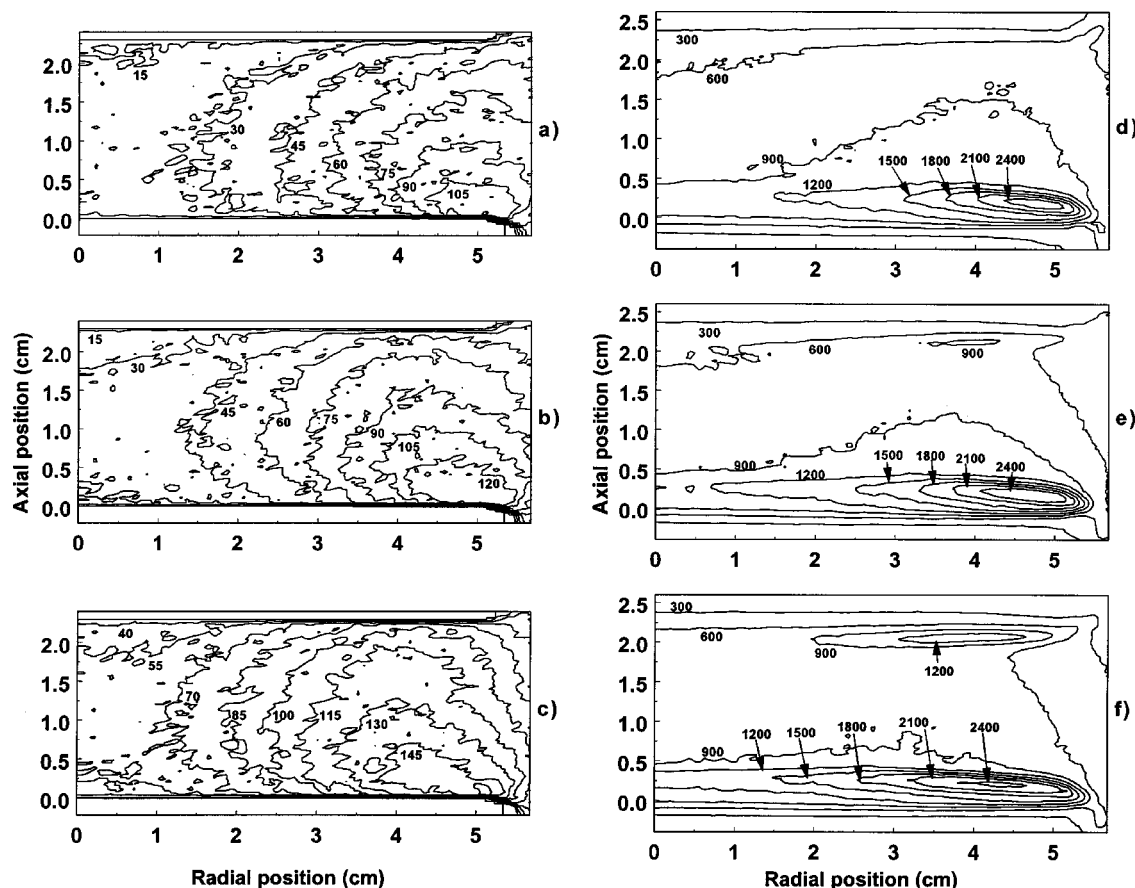


FIG. 8. Contour maps for (a)–(c) PLIF measurement of CF_2 density and (d)–(f) broadband optical emission intensity for a $\text{C}_2\text{F}_6/\text{O}_2$ discharge at 13.3 Pa (100 mTorr), obtained with (a),(d) the tunable load adjusted to minimize $|I_{\text{ue}}|/|I_{\text{pe}}|$; (b),(e) the tunable load short circuited; and (c),(f) the tunable load adjusted to maximize $|I_{\text{ue}}|/|I_{\text{pe}}|$. Load settings, currents, and powers are given in Table II.

also maximized. At 13.3 Pa (100 mTorr), changes in the sheath thickness and associated changes in the emission near the upper electrode are visible to the naked eye, and can be used to find the tuning positions which produce the minimum and maximum $|I_{\text{ue}}|/|I_{\text{pe}}|$. At higher pressures, changes near the upper electrode are hard to resolve by eye, but changes in the emission near the upper ground shield can be used instead.

Because the $\text{C}_2\text{F}_6/\text{O}_2$ mixtures are more electronegative than the CF_4/O_2 mixtures, the “collapse” of the discharge occurs at lower pressures in $\text{C}_2\text{F}_6/\text{O}_2$ discharges than in CF_4/O_2 discharges. PLIF, emission, and electrical data obtained at 53.3 Pa (400 mTorr) in $\text{C}_2\text{F}_6/\text{O}_2$ reflected an intermediate state of collapse, between the data obtained at 66.7 Pa (500 mTorr) CF_4/O_2 and at 133 Pa (1000 mTorr) CF_4/O_2 . Data obtained at 133 Pa (1000 mTorr) of $\text{C}_2\text{F}_6/\text{O}_2$ were even more collapsed than in 133 Pa (1000 mTorr) of CF_4/O_2 .

The radial nonuniformity of the CF_2 density can be quantified using the axially averaged data shown in Fig. 5. One figure of merit for the radial nonuniformity is obtained by taking the ratio of the highest and lowest axially averaged values observed over the region from the center ($r=0$) out to the edge of the electrodes ($r=5.1$ cm). For both CF_4/O_2 and $\text{C}_2\text{F}_6/\text{O}_2$ at 13.3 Pa (100 mTorr), maximizing $|I_{\text{ue}}|/|I_{\text{pe}}|$

produces the most uniform distributions. For example, in Fig. 5(a), the radial nonuniformity decreases from 1.89 with $|I_{\text{ue}}|/|I_{\text{pe}}|$ minimized to 1.65 at short circuit, to 1.30 with $|I_{\text{ue}}|/|I_{\text{pe}}|$ maximized. For $\text{C}_2\text{F}_6/\text{O}_2$, the radial nonuniformity decreases from 4.2 to 3.1 to 2.3, respectively. At higher pressures, maximizing $|I_{\text{ue}}|/|I_{\text{pe}}|$ has smaller effects on the radial nonuniformity. Minimizing $|I_{\text{ue}}|/|I_{\text{pe}}|$ increases the radial nonuniformity.

IV. DISCUSSION

The data in Fig. 5 and the other figures suggest several possible applications. In some chamber-cleaning processes, it might be useful to install a variable load and minimize $|I_{\text{ue}}|/|I_{\text{pe}}|$, to force reactive species outward to clean remote surfaces. In other chamber-cleaning steps designed to clean the central portions of the reactor, it might be useful to maximize $|I_{\text{ue}}|/|I_{\text{pe}}|$, forcing reactive species inward. Using a tunable load to maximize $|I_{\text{ue}}|/|I_{\text{pe}}|$ might also be useful in etching processes, to increase the uniformity of reactive species across the wafer surface.

We believe that the effects we observe are sufficiently general that reactive species other than CF_2 could be controlled by tunable loads, in CF_4/O_2 , $\text{C}_2\text{F}_6/\text{O}_2$, or other gases. Tunable loads have been used previously to control

the rf current in electropositive Ar and Ar/N₂ discharges,^{5,7} in addition to the electronegative discharges studied here. Furthermore, according to fundamental models^{8–10} which do not depend on the gas mixture, an increase in rf current should be accompanied by an increase in the power absorbed by plasma electrons. Finally, although plasma chemistry may be complicated, it is reasonable to believe that an increase in the power absorbed by plasma electrons should result in greater dissociation of the feed gas, and an increase in the density of many if not all reactive species. For example, in previous studies^{2,18} of CF₄/O₂/Ar, C₂F₆/O₂/Ar, and NF₃/Ar discharges, the optical emission intensities of Ar, F, and O lines, measured near the radial center of the reactor, all showed a similar pressure dependence. As the pressure was increased from 6.7 to 267 Pa (50–2000 mTorr) the intensity of each peak was seen to rise and then fall. The maxima in the optical emission intensities coincided with a minimum in the plasma impedance, an impedance phase $\phi_{pe} \approx -40^\circ$, and a maximum in $|I_{ue}|/|I_{pe}|$ (denoted $|I_{ge}|/|I_{pe}|$ in previous work). Models² suggest that the maxima in optical emission intensity occur at the pressure at which power is most efficiently transferred to plasma electrons near the radial center of the reactor. (At lower pressures, power is wasted on ions; at higher pressures the plasma collapses away from the radial center towards the electrode edge.) Similarly, the feed gas destruction efficiency in CF₄/O₂/Ar, C₂F₆/O₂/Ar, and NF₃/Ar discharges, measured by mass spectrometry, is maximized when $|I_{ue}|/|I_{pe}|$ is high and $\phi_{pe} \approx -40^\circ$.¹⁸ In a different reactor, in NF₃/Ar discharges, Ar and F optical emission intensities were correlated with each other and with the etch rate of SiO₂ and silicon nitride.¹⁹ In SF₆/Ar discharges, by seeking conditions at which $|Z_{pe}|$ was minimized and ϕ_{pe} was near -45° , the etch rate of alpha silicon carbide was maximized.²⁰ These results suggest that etch rates depend strongly on the amount of power absorbed by plasma electrons. Thus, if a tunable load is able to control the spatial uniformity of electron heating, it should also be able to control the spatial uniformity of etching or chamber-cleaning rates.

One limitation of our tunable load was its inability to increase $|I_{ue}|$ and $|I_{ue}|/|I_{pe}|$ at higher pressures. Presumably this is because at high pressures the path through which current flows to the upper electrode is largely resistive, not capacitive. Although the tunable load can be tuned to cancel the capacitive impedance of the sheath at the upper electrode, it cannot cancel resistive impedances associated with the sheath or with adjacent regions of the plasma. This may be an important limitation, since chamber-cleaning processes may operate at pressures at or above 133 Pa (1000 mTorr). Furthermore, the trend towards more resistive plasma impedances at increasing pressures are observed not only in CF₄/O₂ and C₂F₆/O₂, but also in Cl₂,²¹ SF₆,^{22–24} NF₃,²³ CF₄,²⁴ and mixtures of Ar with CF₄,²⁵ C₂F₆,²⁵ SF₆,^{20,25,26} CF₃Cl,²⁷ and NF₃.^{2,18,19,28} The trend towards increasing resistance at higher pressures can be counteracted by increasing the rf power.¹⁹ Interestingly, for extremely electronegative NF₃/Ar discharges, at 50%–75% NF₃ at pressures of

200–266 Pa (1.5–2.0 Torr), the plasma impedance, Z_{pe} , begins to become capacitive again, just before the plasma goes out completely.^{2,19,28} It is possible that a tunable load might be of use in this regime, but we did not investigate such extremely electronegative plasmas.

In contrast, the minimum values of $|I_{ue}|$ and $|I_{ue}|/|I_{pe}|$ are limited by resistances outside of the discharge, within the electrode assembly or the tunable load. The resistance of the coil in our variable load was low enough to obtain very low values of $|I_{ue}|/|I_{pe}|$, and coils with even lower resistances are available. Lowering the coil resistance has the additional benefit of reducing the power lost in the load.

Finally, it should be realized that even when one is operating a plasma reactor without a tunable load, the stray impedance elements contributed by the reactor itself and elements in the circuitry that powers the reactor may affect the path taken by rf currents in the plasma. There is no reason to believe that the stray impedances are optimized to direct rf currents to appropriate surfaces, so further study of reactor electrical characteristics may be warranted. At the very least, to ensure the greatest process reproducibility and stability, one should make sure that reactor electrical characteristics are reproducible and stable. The greatest irreproducibility would occur in a reactor that happened to be operating near a series or parallel resonance. This is not as unlikely as it may seem. As process conditions vary, sheath capacitances will change, perhaps coming into or out of resonance with external inductances. Furthermore, movable parts within the system may unintentionally act as variable-impedance elements. Indeed, in one commercial parallel-plate system equipped with a movable electrode, such resonances have been observed.²⁹ When the gap between the electrodes was set to a particular value, the spatial characteristics of argon plasmas changed dramatically, simultaneous with a change in the amount of current collected at the grounded electrode. Evidently, moving the electrode in that system produced a change in one or more parasitic inductances, which, at a particular position, came into resonance with a capacitive impedance. Also, for reactors in which both electrodes are powered, one should consider that the matching network on one electrode can function as a variable load, affecting the path taken by rf current injected at the opposite electrode. Resonances in such systems could produce confusing and undesirable instabilities. Proper consideration of current steering effects of the type observed here could thus lead to process improvements in such systems.

V. CONCLUSIONS

The spatial distribution of the CF₂ radical in CF₄/O₂ and C₂F₆/O₂ plasmas in a parallel-plate reactor can be controlled by attaching a variable-impedance load between the unpowered electrode and ground. When the net inductive impedance of the load is adjusted to be equal and opposite to the impedance of stray capacitances in parallel with the load, the rf current flowing into the plasma at the powered electrode is steered away from the load electrode to other reactor surfaces, such as the ground shields of both electrodes. This

produces a shift in regions of electron heating, intense optical emission, and high CF_2 density radially outward from the center of the reactor, toward more remote surfaces. When the impedance of the load is adjusted to be equal and opposite to the capacitive impedance of the sheath at the load electrode, the load electrode receives more rf current than it does when the electrode is grounded. This causes regions of electron heating, intense optical emission, and high CF_2 density to shift radially inward, and the distribution of CF_2 across the electrode surfaces to become more radially uniform. At the highest pressure, 133 Pa (1000 mTorr), we were unable to maximize the current at the load electrode. At this pressure, the capacitance of the sheath at the load electrode is dominated by the sheath resistance or the resistance of adjacent regions of the plasma, which cannot be canceled by the variable load.

The relations between rf current, electron heating, optical emission, and radical creation, which are responsible for the effects we observe, appear to be sufficiently general to apply to other radicals and other gas mixtures. Thus, variable loads show promise for use in several different types of applications. Variable loads could be used to direct reactive species in chamber-cleaning plasmas to the surfaces most in need of cleaning, or to increase the radial uniformity of reactive species in etching plasmas. Current steering effects of the kind observed in this article may also be produced by unintentional electrical resonances in plasma reactors. By careful consideration of the electrical characteristics of reactors and the circuitry that powers them, such resonances could be suppressed or eliminated, resulting in improvements in process stability and reproducibility.

¹T. Streif, G. DePinto, S. Dunnigan, and A. Atherton, *Semicond. Int.* **20**, 129 (1997).

²M. A. Sobolewski, J. G. Langan, and B. S. Felker, *J. Vac. Sci. Technol. B* **16**, 173 (1998).

³K. L. Steffens and M. A. Sobolewski, *J. Vac. Sci. Technol. A* **17**, 517 (1999).

⁴P. J. Hargis, Jr. *et al.*, *Rev. Sci. Instrum.* **65**, 140 (1994).

⁵J. S. Logan, *IBM J. Res. Dev.* **14**, 172 (1970).

⁶J. H. Keller and W. B. Pennebaker, *IBM J. Res. Dev.* **23**, 3 (1979).

⁷A. Lousa and S. Gimeno, *J. Vac. Sci. Technol. A* **15**, 62 (1997).

⁸M. A. Lieberman and A. J. Lichtenberg, *Principles of Plasma Discharges and Materials Processing* (Wiley, New York, 1994).

⁹M. A. Lieberman, *IEEE Trans. Plasma Sci.* **16**, 638 (1988).

¹⁰V. A. Godyak, R. B. Piejak, and B. M. Alexandrovich, *IEEE Trans. Plasma Sci.* **19**, 660 (1991).

¹¹M. A. Sobolewski, *IEEE Trans. Plasma Sci.* **23**, 1006 (1995).

¹²B. K. McMillin and M. R. Zachariah, *J. Vac. Sci. Technol. A* **15**, 230 (1997).

¹³B. K. McMillin and M. R. Zachariah, *J. Appl. Phys.* **77**, 5538 (1995).

¹⁴The identification of commercial materials and their sources is made to describe the experiment adequately. In no case does this identification imply recommendation by the National Institute of Standards and Technology nor does it imply that the instrument is the best available.

¹⁵M. A. Sobolewski, *J. Vac. Sci. Technol. A* **10**, 3550 (1992).

¹⁶R. A. Waldron, *Theory of Guided Electromagnetic Waves* (Van Nostrand Reinhold, New York, 1969).

¹⁷D. S. King, P. K. Schenck, and J. C. Stephenson, *J. Mol. Spectrosc.* **78**, 1 (1979).

¹⁸W. R. Entley, J. G. Langan, B. S. Felker, and M. A. Sobolewski (unpublished).

¹⁹J. G. Langan, B. S. Felker, S. W. Rynders, and S. E. Beck, *J. Vac. Sci. Technol. A* **16**, 2108 (1998).

²⁰J. D. Scofield, P. Bletzinger, and B. N. Ganguly, *Appl. Phys. Lett.* **73**, 76 (1998).

²¹Y. T. Lee, M. A. Lieberman, A. J. Lichtenberg, F. Bose, H. Baltes, and R. Patrick, *J. Vac. Sci. Technol. A* **15**, 113 (1997).

²²R. Foest, J. K. Olthoff, R. J. Van Brunt, E. C. Benck, and J. R. Roberts, *Phys. Rev. E* **54**, 1876 (1996).

²³B. Andries, G. Ravel, and L. Peccoud, *J. Vac. Sci. Technol. A* **7**, 2774 (1989).

²⁴J. W. Butterbaugh, L. D. Baston, and H. H. Sawin, *J. Vac. Sci. Technol. A* **8**, 916 (1990).

²⁵P. Bletzinger, *J. Appl. Phys.* **67**, 130 (1990).

²⁶B. E. Thompson and H. H. Sawin, *J. Electrochem. Soc.* **133**, 1887 (1986).

²⁷K. D. Allen, H. H. Sawin, M. T. Mocella, and M. W. Jenkins, *J. Electrochem. Soc.* **133**, 2315 (1986).

²⁸J. G. Langan, S. E. Beck, B. S. Felker, and S. W. Rynders, *J. Appl. Phys.* **79**, 3886 (1996).

²⁹M. A. Sobolewski and M. W. Horn (unpublished).